

Near-field probing of Bloch surface waves in a dielectric multilayer using photonic force microscopy

DANIIL A. SHILKIN,¹ EVGENY V. LYUBIN,¹ IRINA V. SOBOLEVA,^{1,2} AND ANDREY A. FEDYANIN^{1,*}

¹Faculty of Physics, Lomonosov Moscow State University, 119991 Moscow, Russia

²Frumkin Institute of Physical Chemistry and Electrochemistry, Russian Academy of Science, Moscow 119071, Russia

*Corresponding author: fedyanin@nanolab.phys.msu.ru

Received 6 April 2016; accepted 7 April 2016; posted 19 April 2016 (Doc. ID 262041); published 13 May 2016

The potential of photonic force microscopy (PFM) for probing the optical near-field in the vicinity of a dielectric multilayer is demonstrated. An experimental study of Bloch surface waves (BSWs) using PFM is described in detail. The applied technique is based on measuring the BSW-induced gradient force acting on a probe particle combined with precise control of the distance between the particle and the multilayer surface. The BSW-induced potential profile measured using PFM is presented. The force interaction between the probe and the BSW evanescent field is numerically studied. The results indicate that a polystyrene particle with a diameter of 1 μm does not significantly perturb the BSW field and can be used to probe the optical near-field intensity in an elegant, noninvasive manner. © 2016 Optical Society of America

OCIS codes: (350.4855) Optical tweezers or optical manipulation; (230.5298) Photonic crystals; (240.6690) Surface waves.

<http://dx.doi.org/10.1364/JOSAB.33.001120>

1. INTRODUCTION

Optical gradient forces are primarily exploited in trapping applications [1–3] and have been repeatedly used for probing the optical near-field. Photo-induced force microscopy (PIFM) utilizes optical gradient forces acting on a force microscope tip. The electric field distributions of tightly focused laser beams with different polarizations [4] and propagating surface plasmon polaritons [5] have been studied using PIFM. In contrast to tip-based techniques, including PIFM, analyzing the thermal motion of a probe particle in an optical potential based on photonic force microscopy (PFM) [6–8] enables considerably simpler imaging of the optical near-field directly in microfluidic systems [9].

Dielectric multilayers are simple-to-fabricate one-dimensional photonic crystals, which can support surface electromagnetic waves known as Bloch surface waves (BSWs) [10,11]. Due to their high quality factor, BSWs are widely used in sensing applications [12–14]. Similar to plasmonic waveguides, dielectric multilayers are also considered to be a possible platform for two-dimensional integrated optics. BSW refraction, reflection, and focusing schemes have been realized by depositing flat polymer structures on dielectric multilayers [15,16]. Near-field imaging of BSWs has been realized using scanning near-field optical microscopy [17]. We recently reported PFM measurements of BSW-induced optical forces acting on a dielectric microparticle [18,19].

In this work, the potential of PFM to directly probe the optical near-field in the vicinity of a dielectric multilayer is demonstrated. An experimental study of Bloch surface waves using PFM is performed. The BSW-induced forces are determined, and the role of perturbation of the BSW field by the probe is discussed.

2. EXPERIMENTAL TECHNIQUE

In our PFM experiments, optical tweezers are used to localize a probe particle near the dielectric multilayer. The motion of the particle is tracked with and without the BSW. The procedure is repeated at different positions of the optical tweezers trap. Consequently, the BSW-induced potential is obtained for a wide range of distances between the probe and the multilayer surface.

Some technical solutions for performing precise measurements with optical tweezers can be found, for example, in [20–22]. The setup used in our experiments is shown in Fig. 1. The trap is formed by the radiation of a fiber-pigtailed single-mode laser diode 1 emitting a wavelength of 975 nm. The power of the laser output is set to approximately 0.1 W. The output light is collimated by an aspheric lens 2 with a focal length of 18.4 mm into a parallel beam with a diameter of 3.8 mm. The lens is covered with an infrared anti-reflection coating. A neutral optical filter 3 of 10% transmission

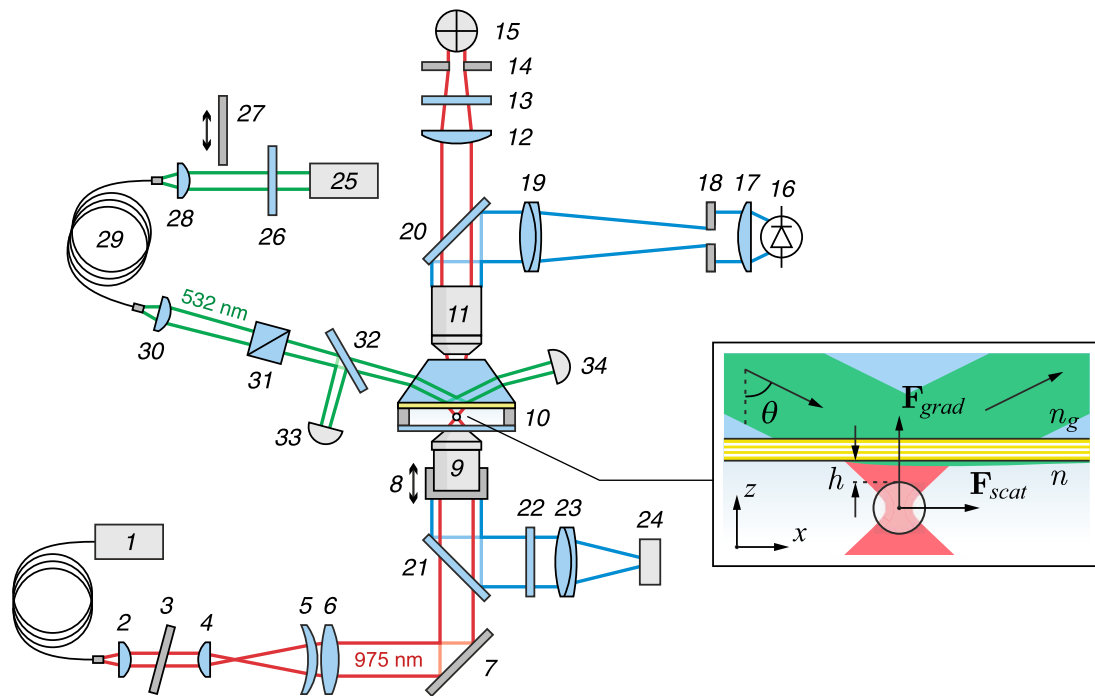


Fig. 1. Experimental setup. 1, fiber-pigtailed 975 nm laser diode; 2, 4–6, 12, 17, 19, 23, 28, 30, lenses; 3, 13, 22, optical filters; 7, mirror; 8, mechanical and piezo translation stage; 9, 11, objective lenses; 10, sample; 14, 18, iris diaphragms; 15, quadrant photodiode; 16, LED; 20, 21, dichroic beamsplitters; 24, CMOS imaging sensor; 25, frequency-doubled Nd:YAG laser; 26, half-wave plate; 27, electromechanical shutter; 29, single-mode polarization-maintaining optical fiber; 31, Glan prism; 32, glass plate; 33, 34, photodiodes. In the inset, a magnified view is presented (not to scale).

prevents the light reflected from the sample from entering the resonator and thus increases the power stability of the laser radiation.

The collimated beam is expanded by an aspheric lens 4 ($f = 25$ mm) and a doublet of a positive meniscus lens 5 and a biconvex lens 6. The focal length of both doublet lenses is approximately 150 mm. Each of the beam expander lenses is covered with an antireflection coating. After expansion, the beam is reflected from a mirror 7 and focused by an Olympus UPlanSApo 60XW water-immersion objective lens 9 with a NA of 1.2 inside a cell 10 filled with a water suspension of polystyrene microbeads with a diameter of 1 μm .

The cell consists of two cover glasses with a refractive index of 1.52 and a thickness of approximately 0.15 mm separated by friction tape with a thickness of 0.2 mm. The bottom side of the upper glass is covered with a photonic crystal sample. To avoid adhesion between the microparticles and the multilayer surface, the commonly used surfactant sodium dodecyl sulfate (SDS) is added. The concentration of SDS in the suspension is 10 mM, which is slightly higher than the critical micelle concentration [23]. The cell is placed on a horizontal stage, which allows manipulation of the sample position relative to the beam axis. The vertical position of the waist is controlled by a mechanical and piezo translation stage 8, on which the objective lens is mounted. The trap position can also be manipulated in three dimensions by moving the lens 4.

The radiation scattered at a particle in the optical tweezers trap is collected by an objective lens 11 with a focal length of 16 mm and a NA of 0.5. The position of the trapped particle is

determined using a quadrant photodiode (QPD) 15, on which an image of the back focal plane of the objective 11 is formed by a 60 mm plano-convex lens 12. The QPD signals are digitized with a sampling rate of 50 kHz. Dichroic optical filters 13 prevent visible radiation from reaching the QPD. Optical radiation forces acting on transparent particles are commonly divided into scattering and gradient components. In the case of BSWs, the scattering component is directed along the BSW propagation, and the gradient component is perpendicular to the multilayer surface, as shown in the inset of Fig. 1. In this work, we are primarily interested in the gradient force, which is directly caused by a nonuniform BSW field distribution and can be obtained by measuring the sum signal of the QPD. Although not used in this work, the difference signals of the QPD can be analyzed to obtain the horizontal force component [18].

The trapped beads are visualized using a standard transmitted light optical microscopy technique. The radiation of an LED 16 is collimated by an aspheric lens 17 ($f = 20$ mm) and passes through a field diaphragm 18 placed in the focal plane of an achromatic doublet 19 ($f = 200$ mm). An image of the field aperture is formed in the cell by the objective 11, providing uniform illumination of the particles. The field of view of the immersion objective 9 is projected onto a CMOS imaging sensor 24 (Thorlabs DCC1545M) by an achromatic doublet 23 with a focal length of 60 mm. Absorptive optical filters 22 are used to prevent laser radiation from reaching the camera. The infrared and visible light are separated by dichroic beamsplitters 20 and 21.

The BSW excitation is realized in the Kretschmann attenuated total internal reflection configuration by using a prism of dense flint glass with an angle of 54.6° and a refractive index of 1.66. The optical contact between the prism and the multilayer is maintained by immersion oil. For excitation of the BSW, the radiation of a frequency-doubled Nd:YAG laser 25 at 532 nm is used. The polarization is controlled by a half-wave plate 26. An electromechanical shutter 27 is used to turn the BSW excitation on and off. The Gaussian mode is selected by a single-mode polarization-maintaining optical fiber 29 with a NA of 0.12 and a mode field diameter of $3.3\ \mu\text{m}$. To couple the laser beam into the fiber, an aspheric lens 28 ($f = 11\ \text{mm}$) is used. At the fiber output, the laser radiation is focused on the multilayer by an aspheric lens 30 ($f = 4.5\ \text{mm}$) into a spot with a diameter of approximately $70\ \mu\text{m}$. The divergence angle in the glass substrate is 0.4° . The beam power at the fiber output is approximately 50 mW, which corresponds to an intensity of $1.6\ \text{kW}/\text{cm}^2$ at the multilayer. A Glan prism 31 is used for additional polarization filtering. The intensity of the radiation beam is controlled by a photodiode 33, on which the beam is directed with a glass plate 32. A photodiode 34 is used to measure the reflectance of the photonic crystal. Components 30–33 are mounted on a rotation stage to control the angle of incidence of the excitation radiation.

The multilayers used were prepared using thermal vacuum deposition. Five pairs of quarter-wavelength layers of ZrO_2 and SiO_2 were deposited on a glass substrate with a refractive index of 1.52. The refractive indices of ZrO_2 and SiO_2 at 532 nm are 1.91 and 1.46, respectively. The actual thicknesses of each of the layers and the refractive indices of the component materials were determined by spectroscopic ellipsometry performed using HORIBA Scientific UVISEL 2. All of the further calculation results were obtained using these data.

Figure 2(a) shows the reflectance calculated using the transfer matrix technique for the multilayers illuminated with s -polarized radiation in the Kretschmann configuration, as a function of wavelength and angle of incidence in the glass substrate. For calculations, one needs to introduce a nonzero absorption; otherwise, total reflectance is obtained even under the BSW resonance conditions. In fact, the BSW excitation leads to a decrease in the reflectance, at least partly, because of the BSW scattering by surface roughness. To take this into account, we introduce effective absorption coefficients. The reflectance shown in Fig. 2(a) was calculated with the absorption coefficients chosen to be $2 \cdot 10^{-4}$ for all of the materials. At normal incidence, the photonic bandgap is centered at approximately 1200 nm. As the angle of incidence increases, the bandgap shifts toward blue. When total internal reflection is achieved at an angle of approximately 61° , a narrow dip appears in the bandgap region corresponding to the excitation of the BSW at the interface between the multilayer and water. At 532 nm, the BSW is excited at an angle of incidence in the glass substrate of 62.1° , corresponding to an angle in the prism of 54.4° .

In the BSW resonance, an electromagnetic field is localized near the surface and decays exponentially behind the multilayer as $E = E_0 L e^{-|z|/d_p}$, where E_0 is the electric field amplitude of the incident light. The field enhancement L calculated for

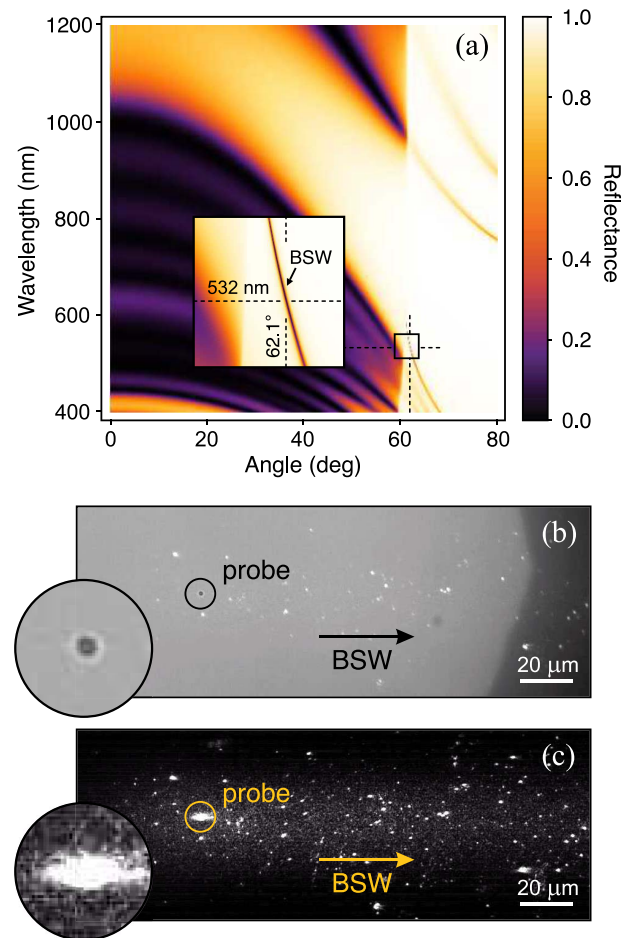


Fig. 2. (a) Calculated reflectance of the multilayer in the Kretschmann scheme. Inset shows magnified BSW dispersion near 532 nm. (b), (c) Photomicrographs of a $1\ \mu\text{m}$ polystyrene particle trapped with optical tweezers in the BSW evanescent field. (b) The photo is taken with additional illumination by an LED. (c) The particle is brought closer to the multilayer surface such that it scatters the BSW radiation. In the insets, magnified images are presented.

resonant excitation is approximately 20. The penetration depth d_p into water is the inverse of the absolute value of the normal wave vector component

$$d_p = \frac{\lambda}{2\pi} \cdot (n_g^2 \sin^2 \theta - n^2)^{-1/2},$$

where λ is the wavelength in vacuum, $n = 1.33$ is the refractive index of water, $n_g = 1.52$ is the refractive index of glass, and $\theta \sim 62^\circ$ is the angle of incidence of the excitation radiation in the glass substrate. Under our experimental conditions, the penetration depth is $d_p \approx 0.4\ \mu\text{m}$, which corresponds to an energy penetration of $0.2\ \mu\text{m}$.

Figures 2(b) and 2(c) present photomicrographs of a polystyrene particle trapped in the BSW evanescent field. In the photo in Fig. 2(b) obtained with additional illumination by the LED 16 (see Fig. 1), an edge of the field aperture 18 is also seen. In Fig. 2(c), the particle is brought closer to the multilayer surface such that it scatters the BSW radiation. The

BSW propagation region is visualized due to scattering by surface roughness.

Precise measurements using PFM require the calibration of the optical tweezers with taking the vicinity of the surface into account. In the first step, the piezoelectric stage is calibrated by mechanical translation. Through the piezoelectric stage, the position of the trapping beam waist can be controlled with nanometer accuracy. However, during long measurements, the multilayer surface can change its position, causing significant uncontrollable changes in the distance between the particle and the surface.

To stabilize the particle position relative to the multilayer surface during the PFM measurements, the following technique is used. First, the dependence of the average QPD sum signal on the position of the trapping beam waist is measured. A typical example of this is shown in Fig. 3(a). Each point in the plot is obtained during 5 s, which is considerably greater than the characteristic time of thermal fluctuations in our experiments, 0.1 s. On the left side of the plot, the waist of the trapping beam is located above the bottom side of the multilayer, and the particle is pressed to the surface and displaced

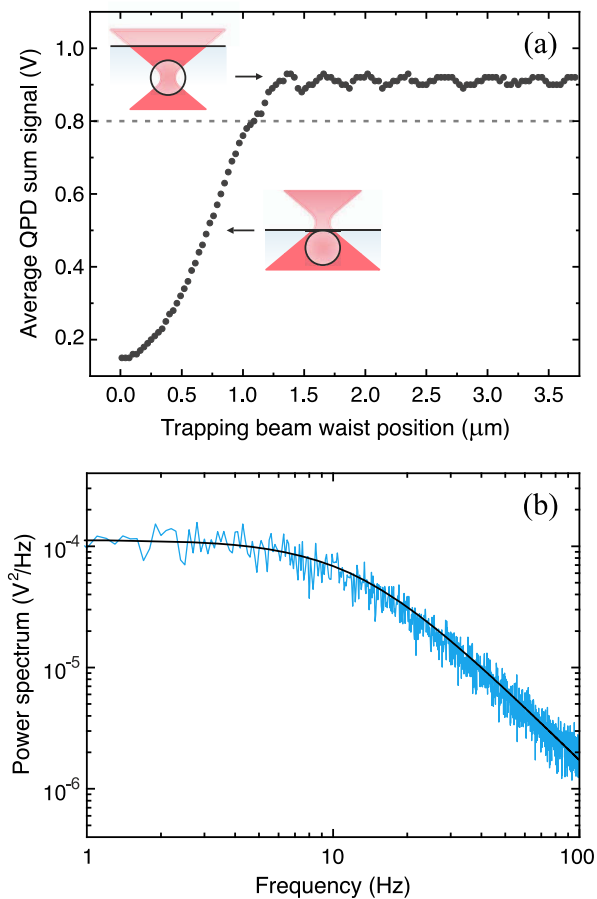


Fig. 3. (a) Average QPD sum signal level as a function of the trapping beam waist position. On the left side of the plot, the waist is above the bottom side of the multilayer, and the particle is pressed to the surface and displaced down the waist. On the right, the beam is focused below the multilayer, and the particle is trapped in the waist. (b) Typical power spectrum of the QPD sum signal (blue) and its approximation by a Lorentzian function (black).

down from the trap. As the waist approaches the surface, its displacement decreases and the QPD signal increases. On the right side of the plot, the waist is located inside the cell, and the particle is trapped near the beam waist. In this case, the equilibrium position relative to the waist center is not significantly changed with the waist displacement, and the average QPD signal remains almost constant. Slight changes in the particle position inside the trap are caused by the reflection of the trapping beam from the multilayer and the presence of the surfactant in the suspension.

After the dependence is obtained, the particle position relative to the multilayer surface can be stabilized as follows. The waist is initially located inside the cell, and the particle is trapped near the waist center. Then, the waist approaches the surface until the average QPD sum signal becomes as small as a certain established value. A possible choice for this parameter is indicated in Fig. 3(a) by the dashed line. After this value is exceeded, the waist is translated by a desired distance inside the cell.

During the measurements, this procedure is repeated every minute, providing a constant average value of the distance between the surface and the equilibrium particle position. Note that one cannot determine the actual distance between the particle and the surface using only the described procedure. Moreover, changing the waist position by a certain value does not guarantee changing the particle equilibrium position by the same value, at least partly, because the reflection of the trapping beam from the multilayer disturbs the optical potential [24,25]. For this reason, the distance between the particle and the surface should be determined independently for every waist position.

When measuring forces with optical tweezers, one typically needs to know two parameters per axis. If the particle displacements are small, the trap potential is harmonic, and the force acting on the trapped particle is proportional to the displacement of the particle equilibrium position. The coefficient of proportionality k , called the trap stiffness, is the first parameter that one needs to obtain from the calibration. The second parameter is the coefficient S of proportionality between the particle displacement and the corresponding change in the QPD signal.

The standard optical tweezers calibration technique allows one to obtain the trap stiffness k and the coefficient S by measuring the power spectrum of the QPD signal [26]. In a harmonic potential, the two-sided power spectral density of the particle coordinate x is

$$G_x(f) = \frac{D/(2\pi^2)}{f_c^2 + f^2},$$

where $D = k_B T / \gamma$ is the diffusion coefficient, $f_c = k / (2\pi\gamma)$ is the corner frequency, k_B is the Boltzmann constant, T is the temperature, and γ is the hydrodynamic drag. If one assumes that $x = SV$, where V is the QPD signal, then the two-sided power spectral density of the QPD signal is calculated as follows:

$$G_V(f) = S^{-2} \frac{D/(2\pi^2)}{f_c^2 + f^2}. \quad (1)$$

Fitting the experimental power spectra by Eq. (1) allows one to obtain S and k for each of the coordinate axes.

When a particle is trapped in the vicinity of a surface, the hydrodynamic friction depends on the distance between the surface and the particle, and Eq. (1) should be transformed as follows:

$$G_V(f) = S^{-2} \frac{D(h)/(2\pi^2)}{f_c^2(h) + f^2}, \quad (2)$$

where $D(h) = \xi(h)k_B T/\gamma$, $f_c(h) = k(h)\xi(h)/(2\pi\gamma)$, and h is the gap between the surface and the particle. The coefficient $\xi(h)$ in the case of motion parallel to the surface is calculated as follows [27]:

$$\xi_{x,y}(h) = 1 - \frac{9}{16} \left(\frac{a}{a+2h} \right) + \frac{1}{8} \left(\frac{a}{a+2h} \right)^3 - \frac{45}{256} \left(\frac{a}{a+2h} \right)^4 - \frac{1}{16} \left(\frac{a}{a+2h} \right)^5,$$

where a is the diameter of the bead. The same coefficient in the case of motion perpendicular to the surface is

$$\xi_z(h) = \frac{12h^2 + 2ah}{12h^2 + 9ah + a^2}.$$

In our measurements, the coefficient S is assumed to be independent of the waist position, and its value is found through extrapolation of values obtained at different waist positions. The coefficients k and h are then determined for every waist position through approximation of single power spectra by Eq. (2). A typical power spectrum is shown in Fig. 3(b). As shown below, knowledge of the stiffness k is not necessary in our experiments. However, the distance h cannot be determined independently of the stiffness.

3. RESULTS AND DISCUSSION

The PFM measurements have been automated using NI LabVIEW 2012. Initially, the waist position is manually set inside the cell at a distance of approximately 1 μm from the multilayer surface. Then, the waist positioning relative to the surface is automatically performed as described above, and the first measurement series begins. Every measurement series consists of three steps. In the first step, data from the QPD are collected for 10 s at the closed position of the shutter 27 (see Fig. 1). Then, the shutter is automatically opened, and the data are collected for 20 s. In the last step, the shutter is closed again, and the data are collected for 10 s. After the series is completed, the waist positioning procedure is performed and the next series begins. For each position of the optical tweezers trap, ten measurement series are carried out. The data from the QPD are converted into units of absolute distance by using the average surface/particle gap h , which is determined independently at every trap position, and the coefficient S , which is the same at all positions. The calibration technique is described in detail above.

The probability density of the particle position $P(z)$ is related to the potential profile $U(z)$ as $P(z) \propto \exp(-U(z)/k_B T)$. The BSW-induced potential U_{BSW} is determined as the difference between the potentials in the presence and absence of the BSW. It is calculated through the probability densities $P_{\text{BSW}}(z)$ and $P_0(z)$ as follows:

$$U_{\text{BSW}}(z)/k_B T = -\ln(P_{\text{BSW}}(z)/P_0(z)) + \text{const.} \quad (3)$$

To avoid large errors, the calculations are performed for the particle positions where both $P_{\text{BSW}}(z)$ and $P_0(z)$ exceed 1% of the maximum values. Typical probability densities in the presence and absence of the BSW are shown in Fig. 4(a). As can be seen, when the BSW is excited, the particle is pushed to the surface of the multilayer, and the trap becomes stiffer. Figure 4(b) presents the corresponding potential profiles and Fig. 4(c) presents their difference.

After the potential profile is obtained at one position of the optical tweezers trap, the procedure is repeated at other positions. Consequently, the BSW-induced potential is obtained for a wide range of distances between the probe and the multilayer surface. The profile presented below was obtained with 14 different trap positions. The total measuring time was about 3 h. Note that the potential Eq. (3) is determined up to a constant, which can be different for various trap positions. We overcame this difficulty by calculating the profile of the derivative $\partial U_{\text{BSW}}(z)/\partial z$ for every trap position and subsequently integrating.

The final result for the BSW-induced potential profile measured by PFM is shown in Fig. 4(d) with blue dots. At distances exceeding 150 nm, the data are fitted to an exponential curve with a decay length of (196 ± 1) nm, which is close to the penetration depth of the BSW energy. The BSW energy distribution calculated using the transfer matrix technique is indicated by the solid black curve. A maximum force value of approximately 0.2 pN is recorded at a distance of 150 nm. At smaller distances, the potential deviates from the exponential curve. This behavior is most likely related to the presence of the surfactant in the suspension, which has not been taken into account either in the calculations or in the calibration process. Electrostatic forces affecting the short-range potential have been assumed to be independent of the presence of the BSW, whereas the distribution of SDS can be significantly disturbed by the BSW field. The difference between the potentials in the presence and absence of the BSW can be contributed by this redistribution. Thermal effects can also cause the potential perturbation at small distances from the multilayer surface.

In the range between 400 and 500 nm, there are fewer experimental points. This result is related to the presence of the reflection of the optical tweezers beam from the multilayer. When the waist is formed at the corresponding distance from the surface, the potential has two local minima because of the formation of the standing wave, and the particle tends to be either closer or farther from the surface than at this position.

A potential profile obtained using PFM can be recalculated for mapping the near-field intensity. If the probe is considerably smaller than the wavelength, it behaves as a point dipole and the potential profile is simply proportional to the intensity. In the case of highly localized electromagnetic fields, the dipole approximation can be used for any particle size [28]. Although this technique is not strictly applicable to the case of evanescent fields, the results obtained justify its use. In this approximation, the energy of interaction between a particle and an electromagnetic field is calculated by integrating the unperturbed field intensity over the particle volume:

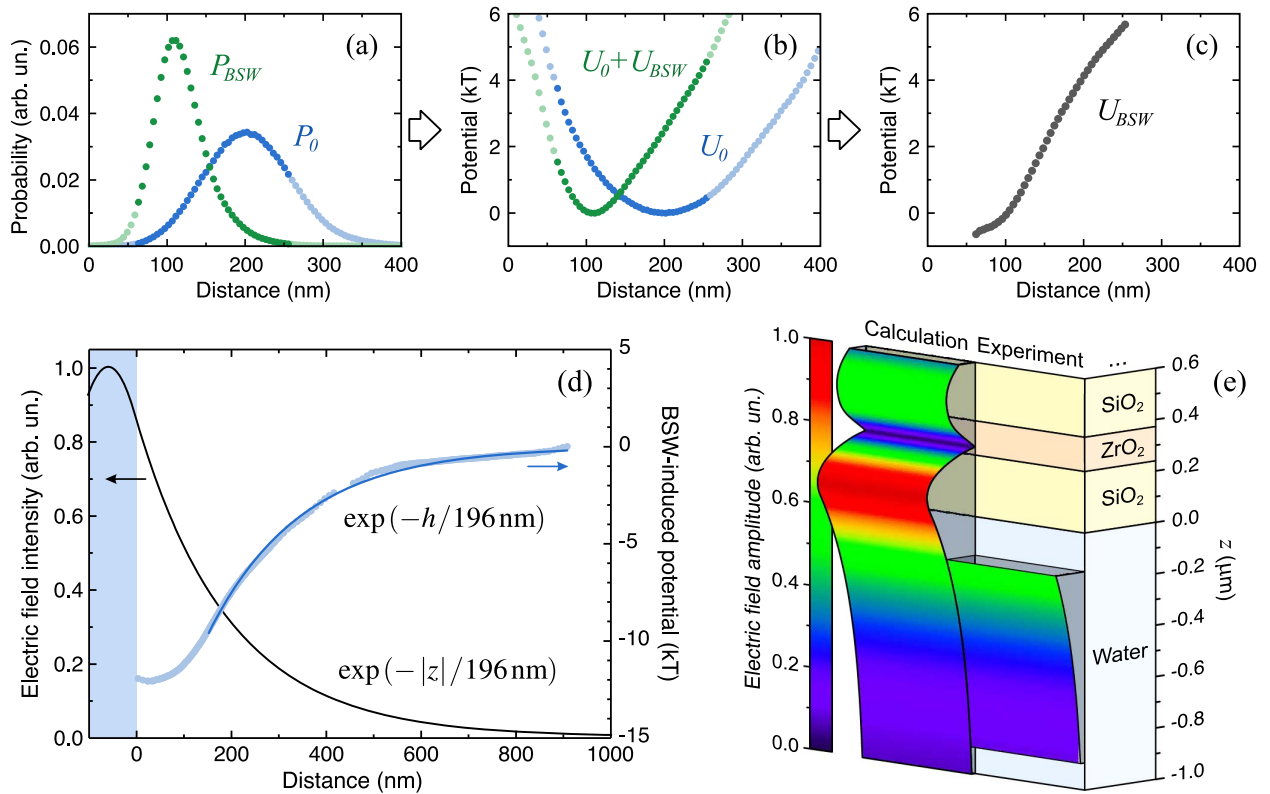


Fig. 4. (a)–(c) PFM results obtained at one position of the optical tweezers trap. (a) Probability densities of the particle position in the presence (green) and absence (blue) of the BSW. (b) Potential profiles in the presence (green) and absence (blue) of the BSW. (c) BSW-induced potential profile. (d) Electric field intensity distribution in the BSW (black) and BSW-induced potential profile measured by PFM as a function of the particle/multilayer gap (blue dots). An exponential fit of the potential at $h > 150$ nm is indicated by the solid blue curve. (e) BSW near-field distribution calculated using the transfer matrix technique (left) and extracted from the PFM measurements (right).

$$U = -\frac{1}{4} \int \alpha E^2 d\mathbf{r}, \quad (4)$$

where $E = E(\mathbf{r})$ is the electric field amplitude, and α is the specific polarizability. In the case of a spherical particle, it is written as follows:

$$\alpha = \frac{3}{4\pi} \frac{m^2 - 1}{m^2 + 2},$$

where m is the ratio of the refractive index of the particle to that of the surrounding medium. The optical gradient force can then be calculated as the gradient of U :

$$\mathbf{F}_{\text{grad}} = -\nabla U.$$

In the BSW evanescent field $E(z) = L(8\pi I/n_g c)^{1/2} e^{-|z|/d_p}$, where I is the intensity of the excitation light, one can obtain an exact solution to the problem in the dipole approximation:

$$U(h) = -\frac{\pi^2 \alpha L^2 I}{2 n_g c} ((a + d_p) e^{-2a/d_p} + (a - d_p)) d_p^2 e^{-2h/d_p}. \quad (5)$$

The potential profile for a probe in an evanescent field is an exponential curve with the same decay length as the electric field intensity distribution. The latter can thus be determined as an exponential fit of the measured potential. It is most clearly demonstrated in Fig. 4(e), where the field amplitude distribution determined by fitting the potential is shown in

comparison with the BSW field calculated using the transfer matrix technique. The calculations are valid when the dipole approximation is applicable. To obtain the exact values of the BSW-induced optical forces acting on a dielectric particle, one needs to determine how the particle perturbs the BSW electromagnetic field. For this purpose, finite-difference time-domain (FDTD) analysis can be used. The optically induced forces are then calculated by integrating the Maxwell stress tensor (MST) over a closed surface enclosing the particle.

For FDTD analysis, we used Lumerical FDTD Solutions. The propagation of a broad-spectrum pulse in the BSW mode in the presence of a $1 \mu\text{m}$ polystyrene bead was simulated, and the Fourier component corresponding to a wavelength of 532 nm was obtained. Figure 5(a) presents the results of the simulation at a surface/particle gap of 100 nm. The BSW propagates from the left to the right, scattering at the particle and inducing the force. The results obtained using the MST technique for different probe sizes at a surface/particle gap of $h = 100$ nm are presented in Fig. 5(b) with dots. The gradient force calculated in the dipole approximation is indicated by the solid black line. For particles smaller than $2 \mu\text{m}$, the results are in good agreement. One can conclude that for these dimensions, the dipole approximation is valid and the potential is proportional to the integral of the electric field intensity over the particle volume. We call this case the “proportional” regime.

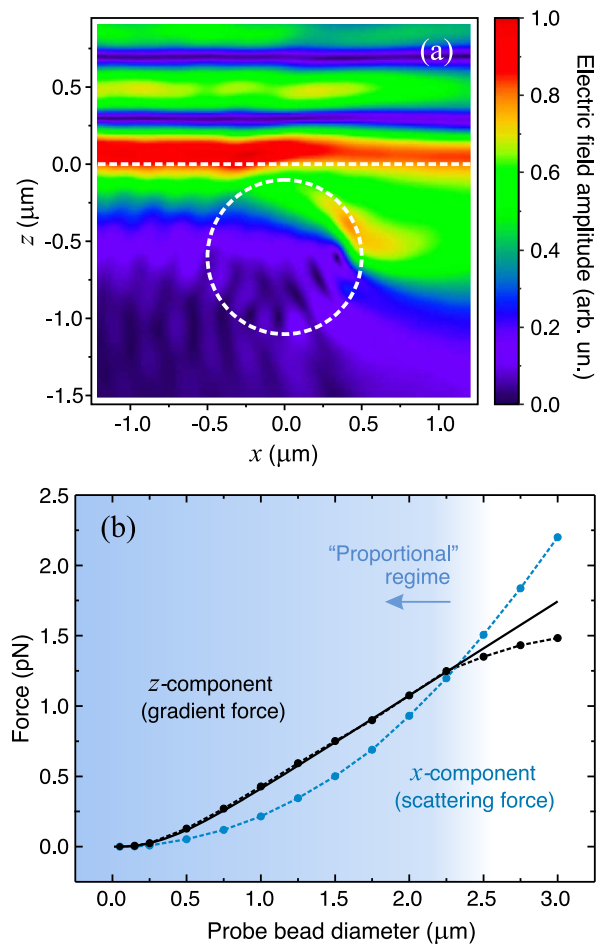


Fig. 5. (a) Electric field amplitude calculated by FDTD simulation at a multilayer/particle gap of 100 nm. (b) The BSW-induced optical force as a function of the particle diameter for plane wave excitation with an intensity of 1 kW/cm^2 at a multilayer/particle gap of 100 nm. The results obtained by integrating the MST are indicated by dots (blue for the x -component, black for the z -component). The gradient force calculated in the dipole approximation is indicated by the solid black curve. In the “proportional” regime indicated in blue, the potential is proportional to the integral of the electric field intensity over the particle volume.

The fact that a $1 \mu\text{m}$ probe does not significantly perturb the BSW field and the BSW-induced optical forces are well described by Eq. (5) ensures the possibility of mapping the BSW near-field. The resolution achievable with this technique is determined not by the probe size and not by the amplitude of its thermal motion inside the trap but by the accuracy of the probe position detection. The case of exponential field distribution is the simplest: the electric field intensity distribution is an exponential curve with the same decay length as the decay length of the field-induced potential. The fact that this quantity from the experiments agrees with the calculated value within an uncertainty of 1 nm further confirms the validity of our approach.

More complex fields can be mapped through PFM measurements in three dimensions. After the particle potential $U(\mathbf{r})$ is obtained, the field distribution $E^2(\mathbf{r})$ can be determined as a

solution of the inverse problem. For this purpose, the three-dimensional Fourier transform should be applied to Eq. (4). As a result, the following relation of the spatial Fourier components of the field $E^2(\mathbf{r})$ and the potential $U(\mathbf{r})$ is obtained:

$$E^2(\mathbf{k}) = \frac{(k/\pi)^3}{2\alpha(ka \cos(ka/2) - 2 \sin(ka/2))} U(\mathbf{k}). \quad (6)$$

One of the difficulties that arises in this case is that the denominator in Eq. (6) is equal to zero if $ka/2 = \tan(ka/2)$ and the corresponding Fourier components of the field cannot be determined. This can be overcome by using a smaller probe or two probes of different sizes.

4. CONCLUSION

Photonic force microscopy has been applied to probe the evanescent field of the Bloch surface wave in a dielectric multilayer. An experimental technique based on using an optically trapped $1 \mu\text{m}$ polystyrene bead as a near-field probe combined with precise control of the probe/multilayer distance has been developed. The BSW-induced potential profile has been measured using PFM. A numerical study revealed that the potential is proportional to the BSW electric field intensity. The results highlight how optical tweezers can be applied for mapping near-field intensity in an elegant, noninvasive manner.

Funding. Russian Foundation for Basic Research (RFBR); Russian Science Foundation (RSF) (15-12-00065).

Acknowledgment. The work was supported by the Russian Science Foundation (experiments, No. 15-12-00065) and by the Russian Foundation of Basic Research (simulations and experimental setup).

REFERENCES

1. A. Ashkin, J. M. Dziedzic, J. E. Bjorkholm, and S. Chu, “Observation of a single-beam gradient force optical trap for dielectric particles,” *Opt. Lett.* **11**, 288–290 (1986).
2. J. E. Curtis, B. A. Koss, and D. G. Grier, “Dynamic holographic optical tweezers,” *Opt. Commun.* **207**, 169–175 (2002).
3. M. Righini, G. Volpe, C. Girard, D. Petrov, and R. Quidant, “Surface plasmon optical tweezers: tunable optical manipulation in the femtonewton range,” *Phys. Rev. Lett.* **100**, 186804 (2008).
4. F. Huang, V. A. Tamma, Z. Mardy, J. Burdett, and H. K. Wickramasinghe, “Imaging nanoscale electromagnetic near-field distributions using optical forces,” *Sci. Rep.* **5**, 10610 (2015).
5. J. Jahng, F. T. Ladani, R. M. Khan, X. Li, E. S. Lee, and E. O. Potma, “Visualizing surface plasmon polaritons by their gradient force,” *Opt. Lett.* **40**, 5058–5061 (2015).
6. E.-L. Florin, A. Pralle, E. H. K. Stelzer, and J. K. H. Hörber, “Photonic force microscope calibration by thermal noise analysis,” *Appl. Phys. A* **66**, S75–S78 (1998).
7. A. Rohrbach, C. Tischer, D. Neumayer, E.-L. Florin, and E. H. K. Stelzer, “Trapping and tracking a local probe with a photonic force microscope,” *Rev. Sci. Instrum.* **75**, 2197–2210 (2004).
8. G. Volpe, R. Quidant, G. Badenes, and D. Petrov, “Surface plasmon radiation forces,” *Phys. Rev. Lett.* **96**, 238101 (2006).
9. C. Pin, B. Cluzel, C. Renaut, E. Picard, D. Peyrade, E. Hadji, and F. de Fornel, “Optofluidic near-field optical microscopy: near-field mapping of a silicon nanocavity using trapped microbeads,” *ACS Photonics* **2**, 1410–1415 (2015).
10. P. Yeh, A. Yariv, and A. Y. Cho, “Optical surface waves in periodic layered media,” *Appl. Phys. Lett.* **32**, 104–105 (1978).

11. W. M. Robertson and M. S. May, "Surface electromagnetic wave excitation on one-dimensional photonic band-gap arrays," *Appl. Phys. Lett.* **74**, 1800–1802 (1999).
12. F. Villa, L. E. Regalado, F. Ramos-Mendieta, J. Gaspar-Armenta, and T. Lopez-Ros, "Photonic crystal sensor based on surface waves for thin-film characterization," *Opt. Lett.* **27**, 646–648 (2002).
13. E. Descrovi, F. Frascella, B. Sciacca, F. Geobaldo, L. Dominici, and F. Michelotti, "Coupling of surface waves in highly defined one-dimensional porous silicon photonic crystals for gas sensing applications," *Appl. Phys. Lett.* **91**, 241109 (2007).
14. Y. Li, T. Yang, S. Song, Z. Pang, G. Du, and S. Han, "Phase properties of Bloch surface waves and their sensing applications," *Appl. Phys. Lett.* **103**, 041116 (2013).
15. T. Sfez, E. Descrovi, L. Yu, M. Quaglio, L. Dominici, W. Nakagawa, F. Michelotti, F. Giorgis, and H. P. Herzig, "Two-dimensional optics on silicon nitride multilayer: refraction of Bloch surface waves," *Appl. Phys. Lett.* **96**, 151101 (2010).
16. L. Yu, E. Barakat, T. Sfez, L. Hvozdar, J. Di Francesco, and H. P. Herzig, "Manipulating Bloch surface waves in 2D: a platform concept-based flat lens," *Light* **3**, e124 (2014).
17. E. Descrovi, T. Sfez, L. Dominici, W. Nakagawa, F. Michelotti, F. Giorgis, and H.-P. Herzig, "Near-field imaging of Bloch surface waves on silicon nitride one-dimensional photonic crystals," *Opt. Express* **16**, 5453–5464 (2008).
18. D. A. Shilkin, E. V. Lyubin, I. V. Soboleva, and A. A. Fedyanin, "Direct measurements of forces induced by Bloch surface waves in a one-dimensional photonic crystal," *Opt. Lett.* **40**, 4883–4886 (2015).
19. D. A. Shilkin, E. V. Lyubin, I. V. Soboleva, and A. A. Fedyanin, "Photonic force microscopy of surface electromagnetic waves in a one-dimensional photonic crystal," *Proc. SPIE* **9548**, 954810 (2015).
20. K. C. Neuman and S. M. Block, "Optical trapping," *Rev. Sci. Instrum.* **75**, 2787–2809 (2004).
21. W. M. Lee, P. J. Reece, R. F. Marchington, N. K. Metzger, and K. Dholakia, "Construction and calibration of an optical trap on a fluorescence optical microscope," *Nat. Protoc.* **2**, 3226–3238 (2007).
22. G. Pesce, G. Volpe, O. M. Maragó, P. H. Jones, S. Gigan, A. Sasso, and G. Volpe, "Step-by-step guide to the realization of advanced optical tweezers," *J. Opt. Soc. Am. B* **32**, B84–B98 (2015).
23. A. Dominguez, A. Fernandez, N. Gonzalez, E. Iglesias, and L. Montenegro, "Determination of critical micelle concentration of some surfactants by three techniques," *J. Chem. Educ.* **74**, 1227–1231 (1997).
24. P. Jákl, M. Šery, J. Ježek, A. Jonáš, M. Liška, and P. Zemánek, "Behaviour of an optically trapped probe approaching a dielectric interface," *J. Mod. Opt.* **50**, 1615–1625 (2003).
25. D. A. Shilkin, E. V. Lyubin, I. V. Soboleva, and A. A. Fedyanin, "Trap position control in the vicinity of reflecting surfaces in optical tweezers," *J. Exp. Theor. Phys. Lett.* **98**, 644–647 (2014).
26. K. Berg-Sørensen and H. Flyvbjerg, "Power spectrum analysis for optical tweezers," *Rev. Sci. Instrum.* **75**, 594–612 (2004).
27. Y. Kazoe and M. Yoda, "Measurements of the near-wall hindered diffusion of colloidal particles in the presence of an electric field," *Appl. Phys. Lett.* **99**, 124104 (2011).
28. T. Tlusty, A. Meller, and R. Bar-Ziv, "Optical gradient forces of strongly localized fields," *Phys. Rev. Lett.* **81**, 1738–1741 (1998).